Tanvir R. Tanim
Department of Mechanical and
Nuclear Engineering,
The Pennsylvania State University,
University Park, PA 16802
e-mail: trt140@psu.edu

Christopher D. Rahn
Professor
Department of Mechanical and
Nuclear Engineering,
The Pennsylvania State University,
University Park, PA 16802
e-mail: cdrahn@psu.edu

Chao-Yang Wang
Professor
William E. Diefenderfer Chair
of Mechanical Engineering,
and Director of the Electrochemical
Engine Center,
Department of Mechanical
and Nuclear Engineering,
The Pennsylvania State University,
University Park, PA 16802
e-mail: cxw31@psu.edu

A Temperature Dependent, Single Particle, Lithium Ion Cell Model Including Electrolyte Diffusion

Low-order, explicit models of lithium ion cells are critical for real-time battery management system (BMS) applications. This paper presents a seventh-order, electrolyte enhanced single particle model (ESPM) with electrolyte diffusion and temperature dependent parameters (ESPM-T). The impedance transfer function coefficients are explicit in terms of the model parameters, simplifying the implementation of temperature dependence. The ESPM-T model is compared with a commercially available finite volume based model and results show accurate matching of pulse responses over a wide range of temperature (T) and C-rates (I). The voltage response to 30 s pulse charge–discharge current inputs is within 5% of the commercial code for $25\,^{\circ}C < T < 50\,^{\circ}C$ at $I \leq 12.5C$ and $-10\,^{\circ}C < T < 50\,^{\circ}C$ at $I \leq 1C$ for a graphite/nickel cobalt manganese (NCM) lithium ion cell. [DOI: 10.1115/1.4028154]

Keywords: lithium ion battery, single particle model (SPM), battery management system (BMS)

1 Introduction

Corporate average fuel economy standards of 54.5 miles per gallon will double the fuel efficiency of the U.S. fleet, save consumers $1.7 trillion in fuel costs, and reduce U.S. oil consumption by 12×10^9 barrels [1]. This fuel efficiency standard is driving the automotive industry to rely more heavily on partially and fully electrified (battery and/or fuel cell) vehicles. Thomas [2] concludes that most of the vehicles in the U.S. will be hybrid electric vehicles (HEVs) and plug in hybrid electric vehicles (PHEVs) by 2034 and 2045, respectively. Li-ion batteries are the leading candidates for HEVs and PHEVs, as they offer 40–50% weight reduction and 30–40% volume reduction along with superior coulometric and energy efficiency compared to their closest rivals, Ni-MH batteries [3]. Hybrids require advanced and real-time BMS that ensure safe and efficient power utilization, estimate state of charge (SOC) and state of health, and balance cell strings [3]. Accurate cell models that capture the fast cell dynamics in HEVs are critical for high performance BMS design. BMS are often based on equivalent circuit models [4–10] that are relatively easy to implement but lack the important underlying physiochemical processes of the cell and require empirical parametrization for precise estimation. Physics-based electrochemical models, on the other hand, include important battery dynamics, are explicitly dependent on the physical cell parameters, and accurately predict the cell response [11,12].

A fundamental electrochemical model [13–15] could be an accurate and reliable candidate for model based BMS design. Computational time and expense of solving the underlying highly nonlinear and coupled partial differential equations (PDEs), however, limits their use in real time BMS applications. Reduced-order models have been developed by many researchers that predict the cell response with varying degrees of fidelity and model complexity. Smith et al. [12,16] obtains a control-oriented, isothermal, reduced seventh-order model in state variable form using residue grouping that predicts internal battery potentials,

concentration gradients, and enables SOC estimation from external current and voltage measurements. The numerical model order reduction process, however, does not provide explicit relationships between the cell internal parameters and the coefficients of the impedance transfer function [17]. Lee et al. [18] extend the work of Smith et al. by obtaining an analytic transfer function for electrolyte phase potential and concentration distribution. Klein et al. [19] propose an isothermal simplified PDE based model that assumes constant electrolyte concentration and approximates solid phase diffusion using three equations for volume average concentration, particle surface concentration, and average concentration, respectively. In subsequent paper [20], temperature effect is included by solving the energy equation and incorporating temperature correction terms, resulting in good agreement with a hybrid drive cycle.

The single particle model (SPM) studied by many researchers [17,21–24] is a simplified, physics-based, fundamental model. The two cell electrodes are modeled by two spherical particles and associated diffusion equations are solved assuming average electrochemical reaction rate. The electrolyte dynamics are completely ignored by assuming instantaneous Li-ion transfer from one electrode to the other, leading to significant error at higher C-rates [17]. Rahimian et al. [25] propose an improved isothermal SPM by adding polynomially approximated electrolyte dynamics. Their improved SPM reduces to 13 differential algebraic equations and are solved in COMSOL Inc., Marcicki et al. [26] recently added first-order truncated electrolyte dynamics to a SPM from cell specific transcendental transfer function.

Most of the previously developed SPMs do not consider the electrolyte dynamics and are isothermal. Few researchers such as Refs. [25] and [26] attempted to incorporate the electrolyte dynamics into the SPM model. On the other hand, isothermal models can be highly inaccurate at low temperatures. A BMS capable of achieving excellent SPM model based SOC estimation at room temperature, for example, would produce erroneous results when cold ($-10\,^{\circ}C$) starts. This paper: (i) incorporates electrolyte dynamics into a conventional, isothermal SPM of a Li-ion cell; (ii) simulates the performance compared to a commercial code (EC Power, AutoLion-ST™); (iii) adds temperature dependent parameters to the model; and (iv) demonstrates the improved

performance of this ESPM-T effect. Integral method analysis (IMA) is used to solve the Li-ion diffusion equation in the electrolyte domain. Advanced order reduction techniques of parabolic diffusion equation such as approximate inertial manifolds and the use of empirical eigen functions can be found in Refs. [27] and [28]. Temperature is an input to the ESPM-T model so the heat transfer dynamics are not included. On boarding a vehicle, the cell temperature can be measured. In the simulated performance comparisons, the cell temperature is provided by AutoLion-ST.

2 Mathematical Modeling

Figure 1 shows the three domains of the pseudo 2D Li-ion cell model: Porous anode with spherical graphite particles, porous separator, and porous cathode with spherical active material particles (e.g., lithium NCM oxide, lithium cobalt oxide (LCO), lithium manganese oxide (LMO), or lithium iron phosphate LFP). The electrolyte is typically 1.2 M LiPF$_6$ in propylene carbonate (PC)/ethylene carbonate (EC)/dimethyl carbonate (DMC) and saturates all three domains. A microporous polymer or gel polymer separator isolates the direct electron path between the positive and negative electrodes, but allows Li-ions to diffuse through. Aluminum (Al) and copper (Cu) foil current collectors are attached at the ends of positive and negative electrodes, respectively.

During discharge, Li-ions deintercalate from the negative electrode

$$\mathrm{Li}_x\mathrm{C} \overset{\text{discharge}}{\rightleftharpoons} \mathrm{C} + x\mathrm{Li}^+ + xe^- \tag{1}$$
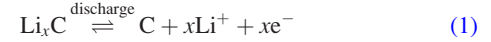
and intercalate into the positive electrode for LMO active material particles

$$\mathrm{Li}_{(1-x)}MO_2 + x\mathrm{Li}^+ \overset{\text{discharge}}{\rightleftharpoons} \mathrm{Li}MO_2 \tag{2}$$
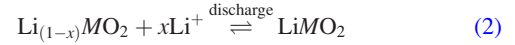
where M stands for a metal. The opposite reactions occur during charge.

2.1 Governing Equations. The electrochemical model of a Li-ion cell can be described by four governing equations: Conservation of Li-ion (Li$^+$) and conservation of charge (e$^-$) in both the solid and electrolyte phases. Conservation of Li$^+$ in a single, spherical, solid phase particle is described by Fick's law of diffusion

$$\frac{\partial c_s}{\partial t} = \frac{D_s}{r^2}\frac{\partial}{\partial r}\left(r^2 \frac{\partial c_s}{\partial r}\right) \tag{3}$$

where $c_s(x, r, t) : (0, L) \times (0, R_s) \times R^+ \to [0, c_{s,\max}]$ is the concentration of Li$^+$ in the solid particle. The model parameters are defined in Table 1. The rate at which ions exit or enter the particle equals the volumetric reaction rate at the particle surface, j^{Li}, and zero at the particle center, written as the boundary conditions

$$\left(\frac{\partial c_s}{\partial r}\right)_{r=0} = 0 \tag{4}$$

$$\left(D_s \frac{\partial c_s}{\partial r}\right)_{r=R_s} = -\frac{j^{\mathrm{Li}}}{a_s F} \tag{5}$$

where $j^{\mathrm{Li}} > 0$ for ion discharge and the interfacial surface area, $a_s = (3\varepsilon_s/R_s)$. Equations (3)–(5) are applied on a continuum basis across both electrodes. The solid phase potential depends on the particle surface concentration, $c_{s,e}(x, t) = c_s(x, R_s, t)$. Diffusion in Cartesian coordinates governs the conservation of Li$^+$ in the electrolyte phase

$$\varepsilon_e \frac{\partial c_e}{\partial t} = D_e^{\mathrm{eff}} \frac{\partial^2 c_e}{\partial x^2} + \frac{1 - t_+^0}{F} j^{\mathrm{Li}} \tag{6}$$

where $c_e(x, t) : (0, L) \times R^+ \to [0, c_{e,\max}]$ is electrolyte concentration and ε_e and D_e are different in each domain (anode, separator, and cathode). The Bruggeman relation $D_e^{\mathrm{eff}} = D_e \varepsilon_e^{1.5}$ accounts for the tortuous path of Li$^+$ transport through the porous electrodes and separator. Ensuring zero flux at the current collectors and continuity of concentration and flux through the adjoining domains within the cell, produces the boundary conditions

$$\left(\frac{\partial c_e^n}{\partial x}\right)_{x=0} = 0 \tag{7}$$

$$\left(D_n^{\mathrm{eff}} \frac{\partial c_e^n}{\partial x}\right)_{x=L_n} = \left(D_s^{\mathrm{eff}} \frac{\partial c_e^s}{\partial x}\right)_{x=L_n} \tag{8}$$

$$c_e^n(L_n, t) = c_e^s(L_n, t) \tag{9}$$

$$\left(D_s^{\mathrm{eff}} \frac{\partial c_e^s}{\partial x}\right)_{x=L_n+L_s} = \left(D_p^{\mathrm{eff}} \frac{\partial c_e^p}{\partial x}\right)_{x=L_n+L_s} \tag{10}$$

$$c_e^n(L_n + L_s, t) = c_e^p(L_n + L_s, t) \tag{11}$$

$$\left(\frac{\partial c_e^p}{\partial x}\right)_{x=L_n+L_s+L_p} = 0 \tag{12}$$
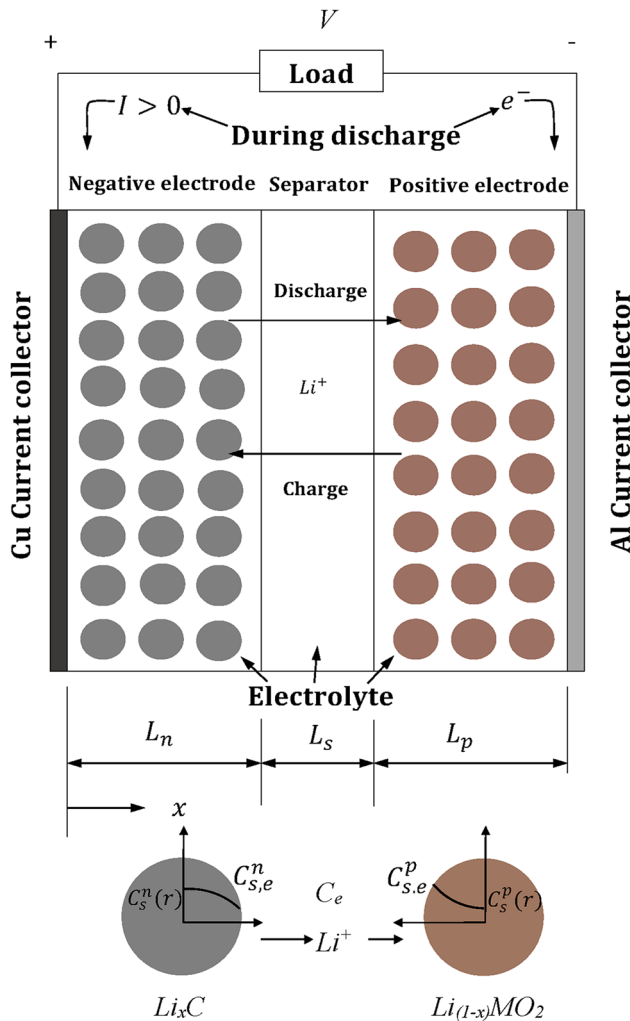

Fig. 1 Schematic diagram of a pseudo 2D Li-ion cell model

Table 1 Model parameters of a 1.78 A h high power gr/NCM Li-ion cell [29–32]

Parameter	Negative electrode	Separator	Positive electrode
Thickness, L (cm)	40×10^{-4}	25×10^{-4}	36.55×10^{-4}
Particle radius, R_s (cm)	5×10^{-4}		5×10^{-4}
Active material volume fraction, ε_s	0.662		0.58
Porosity (electrolyte phase volume fraction), ε_e	0.3	0.4	0.3
Maximum solid phase concentration, $c_{s,max}$ (mol cm^{-3})	31.08×10^{-3}		51.83×10^{-3}
Stoichiometry at 0% SOC, $x_{0\%}$, $y_{0\%}$	0.001		0.955473
Stoichiometry at 100% SOC, $x_{100\%}$, $y_{100\%}$	0.790813		0.359749
Average electrolyte concentration, $c_{e,0}$ (mol cm^{-3})		1.2×10^{-3}	
Exchange current density, $i_{0,ref}$ (A cm^{-2})	2.8×10^{-3}		2.0×10^{-3}
Activation energy of i_0, (kJ mol^{-1})	92		58
Charge transfer coefficient, α_a, α_c	0.5, 0.5		0.5, 0.5
Li$^+$ transference number, t_0^+		0.38	
Film resistance, R_f (Ω cm^2)	0		0
Solid phase Li diffusion coefficient, $D_{s,ref}$ (cm^2 s^{-1})	1.4×10^{-10}		2.0×10^{-10}
Electrode plate area, A (cm^2)		1020.41	
Activation energy of D_s (kJ mol^{-1})	30		25
Contact resistance, R_c (Ω cm^2)		6	

$$U_p(y), (V) \quad -10.72y^4 + 23.88y^3 - 16.77y^2 + 2.595y + 4.563 \quad \text{for} \quad y \in (0,1)$$
$$U_n(x), (V) \quad 0.1493 + 0.8493\exp(-61.79x) + 0.3824\exp(-665.8x) - \exp(39.42x - 41.92) - 0.03131\tan^{-1}(25.59x - 4.099)$$
$$- 0.009434\tan^{-1}(32.49x - 15.74) \quad \text{for} \quad x \in (0.3, 1)$$

where

$$c_e(x,t) = \begin{cases} c_e^n(x,t) & \text{for} \quad x \in (0, L_n) \\ c_e^s(x,t) & \text{for} \quad x \in (L_n, L_n + L_s) \\ c_e^p(x,t) & \text{for} \quad x \in (L_n + L_s, L) \end{cases}$$

Conservation of charge in the solid phase of each electrode is

$$\sigma^{eff}\frac{\partial^2\phi_s}{\partial x^2} = j^{Li} \tag{13}$$

where solid phase potential

$$\phi_s(x,t) = \begin{cases} \phi_s^n(x,t) & \text{for} \quad x \in (0, L_n) \\ \phi_s^p(x,t) & \text{for} \quad x \in (L_n + L_s, L) \end{cases}$$

The fields at the current collectors are proportional to the applied current and zero at the separator

$$-\sigma_n^{eff}\left(\frac{\partial\phi_s^n}{\partial x}\right)_{x=0} = \sigma_p^{eff}\left(\frac{\partial\phi_s^p}{\partial x}\right)_{x=L} = \frac{I}{A} \tag{14}$$

$$\left(\frac{\partial\phi_s^n}{\partial x}\right)_{x=L_n} = \left(\frac{\partial\phi_s^p}{\partial x}\right)_{x=L_n+L_s} = 0 \tag{15}$$

where $I > 0$ indicates discharge. The effective conductivity of the solid phase σ^{eff} can be calculated from $\sigma^{eff} = \sigma\varepsilon_s$, where σ is the reference conductivity of the active material. The linearized electrolyte phase charge conservation equation [13–15]

$$\kappa^{eff}\frac{\partial^2\phi_e}{\partial x^2} + \frac{\kappa_d^{eff}}{c_{e,0}}\frac{\partial^2 c_e}{\partial x^2} + j^{Li} = 0 \tag{16}$$

has boundary conditions

$$\left(\frac{\partial\phi_e^n}{\partial x}\right)_{x=0} = 0 \tag{17}$$

$$\left[\left(\kappa_n^{eff}\frac{\partial\phi_e^n}{\partial x}\right) + \left(\kappa_{d,n}^{eff}\frac{\partial c_e^n}{\partial x}\right)\right]_{x=L_n} = \left[\left(\kappa_s^{eff}\frac{\partial\phi_e^s}{\partial x}\right) + \left(\kappa_{d,s}^{eff}\frac{\partial c_e^s}{\partial x}\right)\right]_{x=L_n} \tag{18}$$

$$\phi_e^n(L_n, t) = \phi_e^s(L_n, t) \tag{19}$$

$$\left[\left(\kappa_s^{eff}\frac{\partial\phi_e^s}{\partial x}\right) + \left(\kappa_{d,s}^{eff}\frac{\partial c_e^s}{\partial x}\right)\right]_{x=L_n+L_s} = \left[\left(\kappa_p^{eff}\frac{\partial\phi_e^p}{\partial x}\right) + \left(\kappa_{d,p}^{eff}\frac{\partial c_e^p}{\partial x}\right)\right]_{x=L_n+L_s} \tag{20}$$

$$\phi_e^s(L_n + L_s, t) = \phi_e^p(L_n + L_s, t) \tag{21}$$

$$\left(\frac{\partial\phi_e^p}{\partial x}\right)_{x=L_n+L_s+L_p} = 0 \tag{22}$$

where

$$\phi_e(x,t) = \begin{cases} \phi_e^n(x,t) & \text{for} \quad x \in (0, L_n) \\ \phi_e^s(x,t) & \text{for} \quad x \in (L_n, L_n + L_s) \\ \phi_e^p(x,t) & \text{for} \quad x \in (L_n + L_s, L) \end{cases}$$

The Bruggeman relation $\kappa^{eff} = \kappa\varepsilon_e^{1.5}$ calculates the effective ionic conductivity of individual domain. The effective diffusional conductivity

$$\kappa_d^{eff} = \frac{2RT\kappa^{eff}}{F}\left(t_+^0 - 1\right)\left(1 + \frac{d\ln f_\pm}{d\ln c_e}\right) \tag{23}$$

according to concentrated solution theory. Butler–Volmer (B-V) kinetics

$$j^{Li} = a_s i_0\left[\exp\left(\frac{\alpha_a F\eta}{RT}\right) - \exp\left(\frac{\alpha_c F\eta}{RT}\right)\right] \tag{24}$$

couple the four conservation Eqs. (3), (6), (13), and (16) describing the four field variables $c_{s,e}$, c_e, ϕ_s, and ϕ_e. Overpotential

$$\eta = \phi_s - \phi_e - U(c_{s,e}) \tag{25}$$

drives the electrochemical reaction rate. The exchange current density in Eq. (24) depends on the solid particle surface and electrolyte concentrations

$$i_0(x,t) = k(T)c_e^{\alpha_a}\left(c_{s,max} - c_{s,e}\right)^{\alpha_a}c_{s,e}^{\alpha_c} \tag{26}$$

Finally, the cell voltage is

$$V(t) = \phi_s(L,t) - \phi_s(0,t) - \frac{R_c}{A}I(t) \tag{27}$$

Finite difference discretization of the governing Eqs. (3)–(22) can produce hundreds of state equations, requiring expensive computation for on-board estimation and control. To reduce the model order for real-time computations, we use efficient discretization techniques and retain only the most significant dynamics of the full order model.

2.2 Low-Order ESPM Formulation. In a conventional isothermal SPM, current density is assumed to be uniformly distributed across each electrode. Thus, all the active material particles are in parallel and each electrode can be replaced by a single spherical particle with radius R_s but Li-ion storage capacity is equal to the electrode storage capacity. The electrolyte dynamics are neglected, resulting in under predicted voltage swings and transients. The assumptions of the ESPM are: (i) infinite solid phase conductivity in the individual electrodes resulting no ohmic loss, (ii) uniform current distribution in the individual electrodes, (iii) linearized conservation equations in the electrolyte domain, and (iv) all properties are evaluated at the equilibrium point (at 50% SOC). Assumptions (i), (ii), and (iv) are also used in SPM models.

Conservation of Li in the single electrode particle for the SPM is solved by taking the Laplace transform of the particle diffusion (Eq. (3)) and applying boundary conditions (4) and (5). The solid state diffusion impedance transfer function at the particle surface of a spherical particle is

$$\frac{\tilde{C}_{s,e}(s)}{J^{Li}(s)} = \frac{1}{a_s F}\left(\frac{R_s}{D_s}\right)\left[\frac{\tanh(\beta)}{\tanh(\beta) - \beta}\right] \tag{28}$$

where $\beta = R_s\sqrt{(s/D_s)}$ and the tilde indicates a small perturbation from the equilibrium condition [33] $c_{s,e}(t) = \bar{c}_{s,e} + \tilde{c}_{s,e}(t)$. Note that at equilibrium, $\bar{\eta}, \bar{j},$ and $\bar{c}_e$ are zero so, tildes are unnecessary. Capital letters indicate a variable has been Laplace transformed. Conservation of charge in the electrode (Eq. (13)) is simplified by integrating in each electrode domain and applying the boundary conditions (14) and (15). The final transfer functions are

$$\frac{J_n^{Li}(s)}{I(s)} = \frac{1}{AL_n} \tag{29}$$

$$\frac{J_p^{Li}(s)}{I(s)} = -\frac{1}{AL_p} \tag{30}$$

where the assumed uniform current distributions are defined as $J_p^{Li}(s) = (1/L_p)\int_{L_n+L_s}^{L} J^{Li}(x,s)dx$ and $J_n^{Li}(s) = (1/L_n)\int_0^{L_n} J^{Li}(x,s)dx$, in the positive and negative electrodes, respectively. Using Eqs. (28)–(30), the solid phase surface concentrations are

$$\frac{\tilde{C}_{s,e}^p(s)}{I(s)} = -\frac{1}{a_s^p FAL_p}\left(\frac{R_s^p}{D_s^p}\right)\left[\frac{\tanh(\beta^p)}{\tanh(\beta^p) - \beta^p}\right] \tag{31}$$

$$\frac{\tilde{C}_{s,e}^n(s)}{I(s)} = \frac{1}{a_s^n FAL_n}\left(\frac{R_s^n}{D_s^n}\right)\left[\frac{\tanh(\beta^n)}{\tanh(\beta^n) - \beta^n}\right] \tag{32}$$

in the positive and negative electrodes, respectively. These transcendental transfer functions are infinitely differentiable and can be discretized using a Padé approximation [34,35]. Prasad and Rahn [17] experimentally validated a third-order Padé approximation with a 10 Hz bandwidth, sufficiently high for current electric vehicle applications. The third-order Padé approximations of Eqs. (31) and (32) are

$$\frac{\tilde{C}_{s,e}^p(s)}{I(s)} = \frac{21\left[\dfrac{1}{a_s^p FAR_s^p L_p}s^2 + \dfrac{60D_s^p}{a_s^p FA[R_s^p]^3 L_p}s + \dfrac{495[D_s^p]^2}{a_s^p FA[R_s^p]^5 L_p}\right]}{s^3 + \dfrac{189D_s^p}{[R_s^p]^2}s^2 + \dfrac{3465[D_s^p]^2}{[R_s^p]^4}s} \tag{33}$$

$$\frac{\tilde{C}_{s,e}^n(s)}{I(s)} = -\frac{21\left[\dfrac{1}{a_s^n FAR_s^n L_n}s^2 + \dfrac{60D_s^n}{a_s^n FA[R_s^n]^3 L_n}s + \dfrac{495[D_s^n]^2}{a_s^n FA[R_s^n]^5 L_n}\right]}{s^3 + \dfrac{189D_s^n}{[R_s^n]^2}s^2 + \dfrac{3465[D_s^n]^2}{[R_s^n]^4}s} \tag{34}$$

The linearized B-V Eq. (24) is

$$\frac{\eta(s)}{J^{Li}(s)} = \frac{R_{ct}}{a_s} \tag{35}$$

where the charge transfer resistance, $R_{ct} = (RT/i_0(\alpha_a + \alpha_c)F)$.

Combining Eqs. (29), (30), and (35),

$$\frac{\eta_p(s)}{I(s)} = -\frac{R_{ct}^p}{a_s^p}\frac{1}{AL_p} \tag{36}$$

$$\frac{\eta_n(s)}{I(s)} = \frac{R_{ct}^n}{a_s^n}\frac{1}{AL_n} \tag{37}$$

Combining Eqs. (25) and (27) and linearizing around an equilibrium produces the voltage deviation

$$\tilde{V}(t) = \eta_p(L,t) - \eta_n(0,t) + \phi_e(L,t) - \phi_e(0,t) + \frac{\partial U_p}{\partial c_{s,e}}\tilde{c}_{s,e}^p(L,t)$$
$$- \frac{\partial U_n}{\partial c_{s,e}}\tilde{c}_{s,e}^n(0,t) - \frac{R_c}{A}I(t) \tag{38}$$

where R_c is the contact resistance and the negative terminal is assigned as ground.

Taking the Laplace transform of Eq. (38) produces the impedance transfer function

$$\frac{\tilde{V}(s)}{I(s)} = \frac{\eta_p(L,s)}{I(s)} - \frac{\eta_n(0,s)}{I(s)} + \frac{\Delta\phi_e(L,s)}{I(s)} + \frac{\partial U_p}{\partial c_{s,e}}\frac{\tilde{C}_{s,e}^p(L,s)}{I(s)}$$
$$- \frac{\partial U_n}{\partial c_{s,e}}\frac{\tilde{C}_{s,e}^n(0,s)}{I(s)} - \frac{R_c}{A} \tag{39}$$

The open circuit potential (OCP) slopes $(\partial U_p/\partial c_{s,e})$ and $(\partial U_n/\partial c_{s,e})$ can be evaluated at any SOC from the empirically measured OCP functions for the cathode and anode, respectively. In Eq. (39), the voltage associated with the electrolyte dynamics $[\Delta\phi_e(L,s)/I(s)]$ is calculated from the linearized Li-ion species conservation equation Eq. (16) assuming the reaction rate is equal to the average volumetric reaction rates in Eqs. (29) and (30). IMA [3,24,36–38] is used to solve the Li-ion conservation Eq. (6) across the three domains of the cell. Substituting Eqs. (29) and (30) into Eq. (6) for the anode, separator and cathode,

$$\varepsilon_{e,n}sC_e^n(s) - D_n\frac{\partial^2 C_e^n(s)}{\partial x^2} - b_1 I(s) = 0 \quad \text{for} \quad x \in (0, L_n) \tag{40}$$

$$\varepsilon_{e,s}sC_e^s(s) - D_s\frac{\partial^2 C_e^s(s)}{\partial x^2} = 0 \quad \text{for} \quad x \in (L_n, L_n + L_s) \tag{41}$$

$$\varepsilon_{e,p}sC_e^p(s) - D_p\frac{\partial^2 C_e^p(s)}{\partial x^2} + b_2 I(s) = 0 \quad \text{for} \quad x \in (L_n + L_s, L) \tag{42}$$

where $b_1 = \left(1 - t_+^0/\mathrm{FAL}_n\right)$, $b_2 = \left(1 - t_+^0/\mathrm{FAL}_p\right)$, and the superscript "eff" on diffusivity has been removed for simplicity. In the minimal IMA, the quadratic Li-ion concentration profiles in the individual domains are

$$C_e^n(x,s) = c_{0,n}(s) + c_{1,n}(s)x + c_{2,n}(s)x^2 \quad \text{for} \quad x \in (0, L_n) \quad (43)$$

$$C_e^s(x,s) = c_{0,s}(s) + c_{1,s}(s)x + c_{2,s}(s)x^2 \quad \text{for} \quad x \in (L_n, L_n + L_s) \quad (44)$$

$$C_e^p(x,s) = c_{0,p}(s) + c_{1,p}(s)x + c_{2,p}(s)x^2 \quad \text{for} \quad x \in (L_n + L_s, L) \quad (45)$$

where $c_{0,n}, c_{1,n}, \ldots, c_{2,p}$ are the coefficients of the quadratic concentration distributions in x. Note that Eqs. (43)–(45) are third-order in time/Laplace domain. These quadratic distributions are substituted into Eqs. (40)–(42), integrated and applied the associated boundary conditions (7)–(12). Solving the nine equations for the nine unknown coefficients in Eqs. (43)–(45) yields the transfer functions

$$\frac{C_e^n(s)}{I(s)} = \frac{p_{2,n}(x)s^2 + p_{1,n}(x)s + p_{0,n}}{s\left(q_{3,n}s^2 + q_{2,n}s + q_{1,n}\right)} \quad (46)$$

$$\frac{C_e^s(s)}{I(s)} = \frac{p_{2,s}(x)s^2 + p_{1,s}(x)s + p_{0,s}}{s\left(q_{3,n}s^2 + q_{2,n}s + q_{1,n}\right)} \quad (47)$$

$$\frac{C_e^p(s)}{I(s)} = \frac{p_{2,p}(x)s^2 + p_{1,p}(x)s + p_{0,p}}{s\left(q_{3,n}s^2 + q_{2,n}s + q_{1,n}\right)} \quad (48)$$

where the coefficients $p_{0,n}, p_{1,n}, \ldots, q_{3,n}$ are given in Appendix A. Now substituting Eqs. (29) and (30) into Eq. (16), the electrolyte charge conservation equations in the three domains of the cell are

$$\kappa_n \frac{\partial^2 \phi_e^n(s)}{\partial x^2} + \kappa_{d,n} \frac{\partial^2 C_e^n(s)}{\partial x^2} + b_3 I = 0 \quad (49)$$

$$\kappa_s \frac{\partial^2 \phi_e^s(s)}{\partial x^2} + \kappa_{d,s} \frac{\partial^2 C_e^s(s)}{\partial x^2} = 0 \quad (50)$$

$$\kappa_p \frac{\partial^2 \phi_e^p(s)}{\partial x^2} + \kappa_{d,p} \frac{\partial^2 C_e^p(s)}{\partial x^2} - b_4 I = 0 \quad (51)$$

where $b_3 = (1/AL_n)$, $b_4 = \left(1/AL_p\right)$, $\kappa_{d,n} = \left(\kappa_{d,n}^{\mathrm{eff}}/c_{e,0}\right)$, $\kappa_{d,s} = \left(\kappa_{d,s}^{\mathrm{eff}}/c_{e,0}\right)$, $\kappa_{d,p} = \left(\kappa_{d,p}^{\mathrm{eff}}/c_{e,0}\right)$, and the conductivities are assumed constant in each domain (anode, cathode, and separator). Equations (49)–(51) and their associated boundary conditions, Eqs. (17)–(22), are singular due to the zero flux at $x = 0$ and $x = L_n + L_s + L_p$. This situation can be avoided by defining electrolyte voltage difference relative to $\phi_e(0,s)$ [3,11,16]. We define the electrolyte phase voltage differences

$$\Delta\phi_e^n(x,s) = \phi_e^n(x,s) - \phi_e^n(0,s) \quad \text{for} \quad x \in (0, L_n)$$

$$\Delta\phi_e^s(x,s) = \phi_e^s(x,s) - \phi_e^n(0,s) \quad \text{for} \quad x \in (L_n, L_n + L_s)$$

$$\Delta\phi_e^p(x,s) = \phi_e^p(x,s) - \phi_e^n(0,s) \quad \text{for} \quad x \in (L_n + L_s, L)$$

At this point of the derivation the electrolyte concentration profile in each individual domain of the cell is known and expressed as Eqs. (46)–(48). Integrating Eqs. (49)–(51) with respect to x in the individual cell domains and subtracting $\phi_e^n(0,s)$ gives

$$\kappa_n \Delta\phi_e^n + \kappa_{d,n}\left[C_e^n(x,s) - C_e^n(0,s)\right] + \frac{b_3 I x^2}{2} = C_{1n} x \quad (52)$$

$$\kappa_s \Delta\phi_e^s + \kappa_{d,s}C_e^s(x,s) - \frac{\kappa_s\kappa_{d,n}}{\kappa_n}C_e^n(0,s) = C_{1s}x + C_{2n} \quad (53)$$

$$\kappa_p \Delta\phi_e^p + \kappa_{d,p}C_e^p(x,s) - \frac{\kappa_p\kappa_{d,n}}{\kappa_n}C_e^n(0,s) - \frac{b_4 I x^2}{2} = C_{1p}x + C_{2p} \quad (54)$$

where $C_{1,n}, \ldots, C_{2,p}$ are constants of integration. Equations (52)–(54) are solved analytically using the associated boundary conditions (18)–(22). After further simplification, the electrolyte phase potential difference is

$$\frac{\Delta\phi_e(L,s)}{I(s)} = \frac{R_2 s^2 + R_1 s + R_0}{L_2 s^2 + L_1 s + L_0} \quad (55)$$

The coefficients $R_0, \ldots, L_2$ are listed in Appendix A. Equations (33), (34), (36), (37), and (55) are substituted in Eq. (39) to deduce the final ESPM impedance transfer function

$$\frac{\tilde{V}(s)}{I(s)} = K + \frac{K_1 + K_2}{s}$$
$$+ \frac{b_{00}s^6 + b_{01}s^5 + b_{02}s^4 + b_{03}s^3 + b_{04}s^2 + b_{05}s + b_{06}}{s^6 + a_{01}s^5 + a_{02}s^4 + a_{03}s^3 + a_{04}s^2 + a_{05}s + a_{06}} \quad (56)$$

where the coefficients $a_{01}, \ldots, a_{06}, b_{00}, \ldots, b_{06}, K, K_1, \text{and} K_2$ are explicitly given in terms of the model parameters in Appendix B.

2.3 ESPM With Temperature Effect (ESPM-T). The transfer function (Eq. (56)) is converted to a state space realization using observer canonical form [39] which produces seven ordinary differential equations. For isothermal ESPM simulation at a particular temperature all the coefficients are constants and lsim in MATLAB simulates the test response. For nonisothermal case (ESPM-T) the coefficients are updated with cell temperature obtained from AutoLion-ST output at every time step and simulated using ode45.

For the gr/NCM chemistry simulated in this paper, most significant temperature dependent parameters are solid phase diffusion coefficient, exchange current density, electrolyte diffusion coefficient, electrolyte ionic conductivity, and electrolyte diffusional ionic conductivity. Arrhenius equation

$$\psi = \psi_{\mathrm{ref}} \exp\left[\frac{E_{\mathrm{act},\psi}}{R}\left(\frac{1}{T_{\mathrm{ref}}} - \frac{1}{T}\right)\right] \quad (57)$$

is used to calculate solid particle diffusion coefficient and exchange current density. The temperature dependent property ψ (e.g., D_s^p, D_s^n, and i_0) depends on the reference value and the activation energy $E_{\mathrm{act},\psi}$. The empirical correlations for electrolyte properties are extracted from Valøen and Reimers [40]

$$D_e(T) = 10^{-\left[4.43 + \frac{54}{T - (229 + c_{e,0})} + 0.22c_{e,0}\right]} \quad (58)$$

$$\kappa(T) = c_{e,0}[(-10.5 + 0.074T - 6.96 \times 10^{-5}T^2) + c_{e,0}(0.668 - 0.0178T - 2.8 \times 10^{-5}T^2) + c_{e,0}^2(0.494 - 8.86 \times 10^{-4}T^2)]^2 \quad (59)$$

$$\kappa_{d,i} = \frac{2RT\kappa_i^{\mathrm{eff}}}{F}\left(t_0^+ - 1\right)\left(1 + \frac{d\ln f_\pm}{d\ln c_e}\right) = -\frac{2RT\kappa_i^{\mathrm{eff}}}{F}\left(t_0^+ - 1\right)\nu(T) \quad (60)$$

where $\kappa_i^{\mathrm{eff}} = \kappa(T)\varepsilon_i^{1.5}$ and subscript i denotes individual domain. The empirical correlation

$$\nu(T) = 0.601 - 0.24c_{e,0}^{\frac{1}{2}} + 0.982[1 - 0.0052(T - 293)]c_{e,0}^{\frac{3}{2}} \quad (61)$$
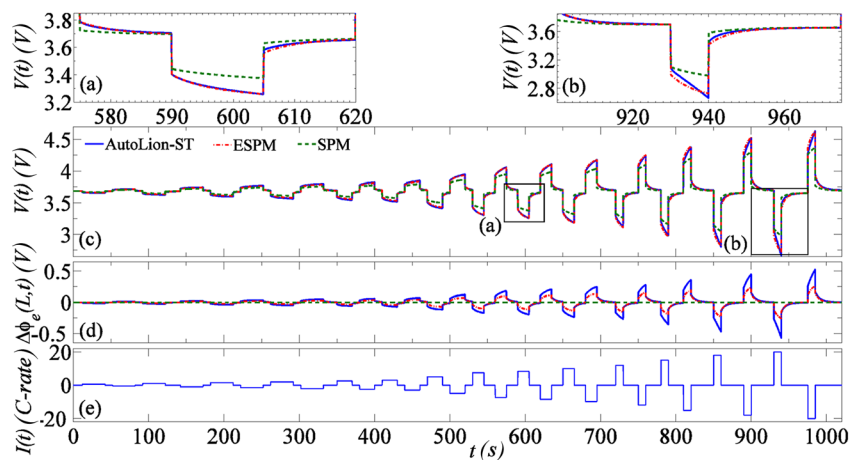
Fig. 2 Voltage response of AutoLion-ST, ESPM, and SPM at 25 °C and 50% initial SOC: (*a*) magnified voltage during 8.5 C discharge pulse (left box in Fig. 2(*c*)), (*b*) magnified voltage during 20 C discharge pulse (right box in Fig. 2(*c*)), (*c*) voltage response, (*d*) electrolyte potential difference, and (*e*) pulse current input

3 Results and Discussion

3.1 Comparison of SPM and ESPM With AutoLion-ST Under Isothermal Conditions. In this work, EC Power's AutoLion-ST is considered to be the truth model and used to compare the accuracy of reduced-order SPM, ESPM, and ESPM-T. AutoLion-ST is a pseudo 2D, fully nonlinear, finite volume based model in MATLAB/SIMULINK. It uses robust numerical algorithms to simulate electrochemical and thermal interactions of Li-ion batteries over a wide range of operating conditions [41]. Figures 2(*a*)–2(*c*) compare the SPM, ESPM and AutoLion-ST voltage responses at 25 °C and 50% initial SOC corresponding to the pulse current input in Fig. 2(*e*). The zoomed in Fig. 2(*a*) shows that the SPM response deviates significantly from the ESPM and AutoLion-ST voltage responses, even at lower C-rates. The ESPM voltage response, however, closely matches AutoLion-ST, including 20 C–10 s pulses (see zoomed view in Fig. 2(*b*)).

Figure 2(*d*) shows the time response of the electrolyte potential $\Delta\phi_e(t) = \phi_e(L,t) - \phi_e(0,t)$ is strongly C-rate dependent. This

internal variable can not be predicted by ECMs. The ESPM, however, is based on the fundamental equations of the cell and internal variables such as $\Delta\phi_e(t)$ can be predicted. The ESPM predicts electrolyte potential difference accurately at low C-rates but has almost 50% (314 mV) error at high C-rates. The quadratic concentration distributions and constant current distributions contribute into this error at higher C-rates. Although $\Delta\phi_e(t)$ is underpredicted by the ESPM, it is a significant improvement over SPM which neglects electrolyte dynamics entirely.

One can tune the SPM contact resistance to account for the unmodeled electrolyte dynamics. At higher C-rates, however, the SPM voltage response overshoots the AutoLion-ST voltage response due to the neglect of electrolyte diffusion dynamics [17]. Although ESPM underpredicts $\Delta\phi_e(t)$ at higher C-rates, the ESPM's voltage accurately matches the AutoLion-ST's voltage (see Fig. 2(*b*)). Overprediction of overpotentials resulting from the linearization of the B-V kinetic equation compensates for the underpredicted $\Delta\phi_e(t)$. The maximum voltage error between the ESPM and AutoLion-ST is 3% (62 mV) for the 20 C–10 s pulse.
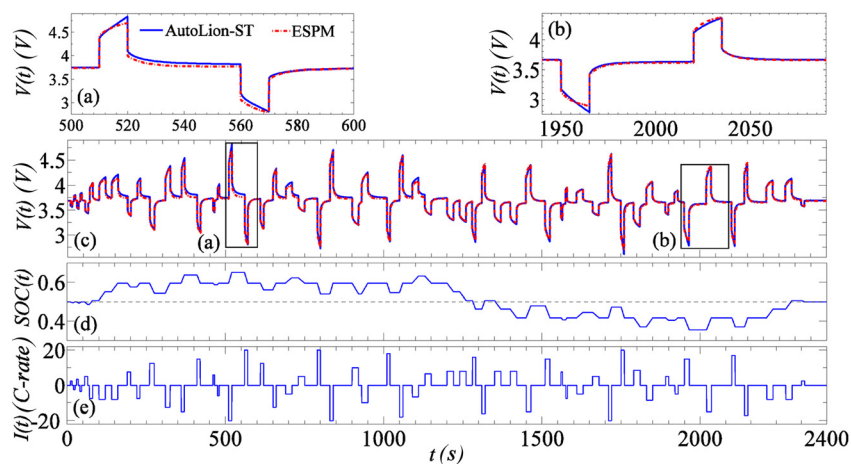

Fig. 3 Voltage response of AutoLion-ST and ESPM at 25 °C and 50% initial SOC: (*a*) magnified voltage during 20 C pulse (left box in Fig. 3(*c*)), (*b*) magnified voltage during 15 C pulse (right box in Fig. 3(*c*)), (*c*) voltage response, (*d*) SOC, and (*e*) pulse current input
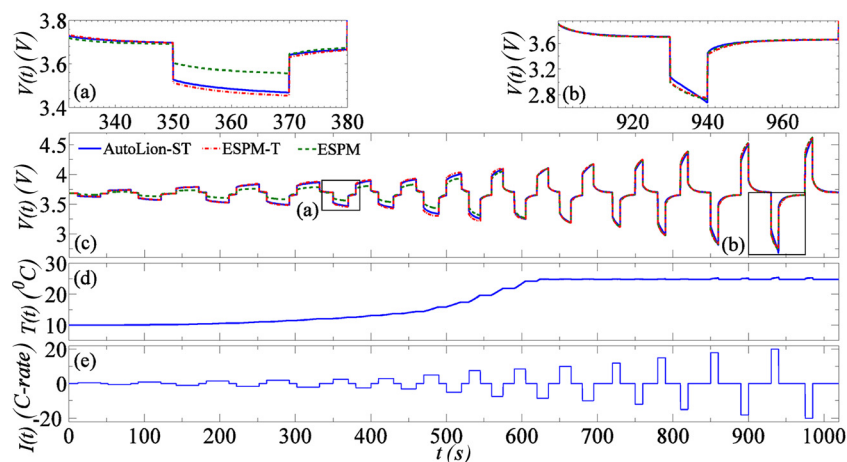
Fig. 4 Voltage response of AutoLion-ST, ESPM, and ESPM-T from 10 °C initial temperature and 50% initial SOC: (*a*) magnified voltage during 2.5 C discharge pulse (left box in Fig. 4(*c*)), (*b*) magnified voltage during 20 C discharge pulse (right box in Fig. 4(*c*)), (*c*) voltage response, (*d*) cell temperature, and (*e*) pulse current input

3.2 Performance of the ESPM Away From the Linearized Point. To test the validity of the ESPM away from the linearization SOC, Fig. 3 simulates a hybrid current cycle operating in a larger 35–65% SOC window. Figure 3(*c*) compares the voltage responses of the ESPM and AutoLion-ST for the current input shown in Fig. 3(*e*). Figure 3(*d*) shows the corresponding SOC swing. Worst case scenarios at the highest and lowest SOCs are presented in the zoomed in Figs. 3(*a*) and 3(*b*), with 20 C–10 s and 15 C–15 s pulses, respectively. The voltage error increases with distance from the linearization point and increasing C-rate. The increased error is caused due the B-V linearization and constant properties assumptions (at 50% SOC) in the ESPM. Nevertheless, the maximum error between the ESPM and AutoLion-ST voltage responses remains less than 4.3% (137 mV) during the entire simulation.

3.3 Comparison of ESPM and ESPM-T With AutoLion-ST Under Nonisothermal Conditions. Figure 4 shows the influence of cell initial temperature on the voltage response by comparing the simulation results from ESPM, ESPM-T, and AutoLion-ST. The cell temperature, as predicted by AutoLion-ST

starts at 10 °C and increases under adiabatic conditions to a temperature limit of 25 °C over the course of the simulation. The AutoLion-ST model includes a cooling system that prevents the cell temperature from exceeding 25 °C. The ESPM is isothermal at 25 °C and the ESPM-T temperature dependent physiochemical properties are updated using the AutoLion-ST output temperature as one could use a temperature sensor on-board a vehicle. ESPM voltage response does not match the AutoLion-ST results at low temperature, even at low C-rates. The highly distributed current along each electrode due to sluggish reaction kinetics, reduced electrolyte diffusivity, and ionic conductivity may attribute the voltage difference at low temperatures. As the cell temperature approaches 25 °C, ESPM and ESPM-T produce identical voltage responses that closely match AutoLion-ST voltage response. The magnified Figs. 4(*a*) and 4(*b*) at 2.5 C and 20 C, respectively, show the relative agreement of these simulation methods. Overall, ESPM-T matches AutoLion-ST to within 3% (62 mV) for the entire 10 °C–25 °C temperature range and up to 20 C rates.

3.4 Operating Range of ESPM-T. Figure 5 shows that the accuracy of the ESPM-T model depends on both current rate and
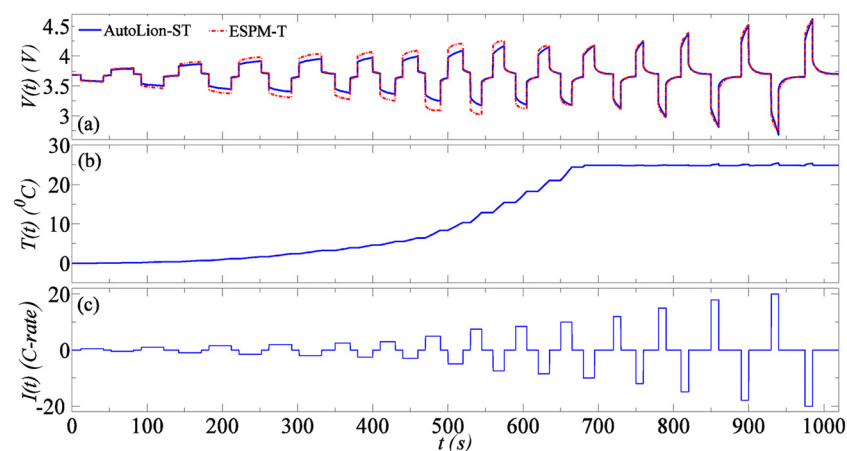

Fig. 5 Voltage response of AutoLion-ST and ESPM-T from 0 °C and 50% initial SOC: (*a*) voltage response, (*b*) cell temperature, and (*c*) pulse current input
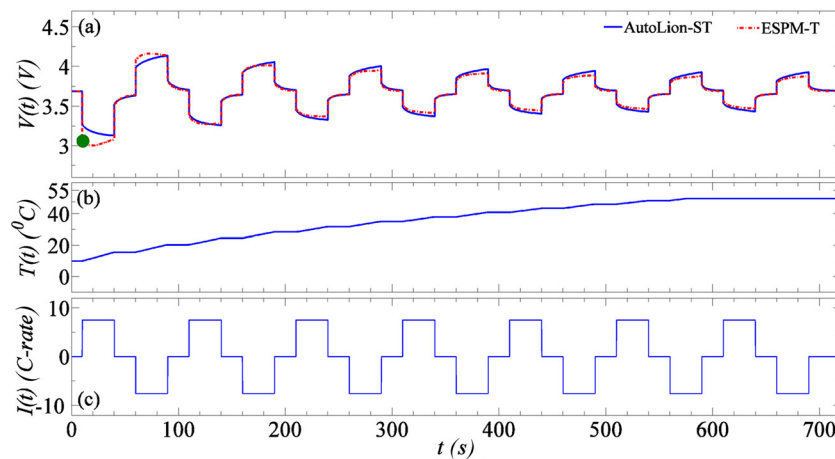
Fig. 6 Voltage response of AutoLion-ST and ESPM-T from 10 °C and 50% initial SOC: (a) voltage response, (b) cell temperature, and (c) 7.5C–30 s hybrid pulse charge– discharge cycle
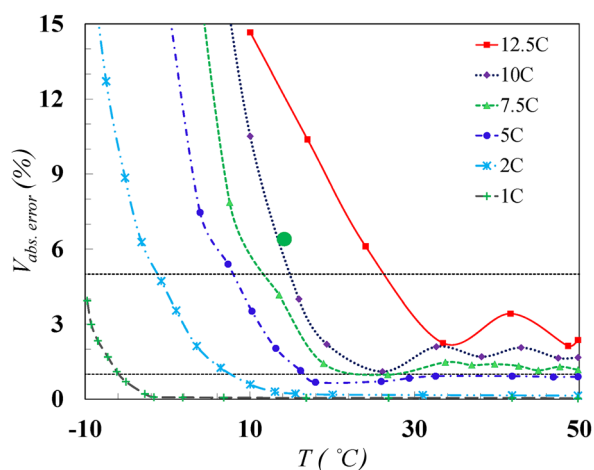

Fig. 7 ESPM-T error relative to AutoLion-ST for different C-rate pulse cycles (see Fig. 6(c)) versus cell temperature. The solid dot corresponds to the dot in Fig. 6(a).

Table 2 Computation time of different Li-ion cell models

Li-ion cell model	Solver	Computation time (s)
AutoLion-ST™	Nonlinear solver	12.5
ESPM-T	ode45	2.5
ESPM	lsim	1.05
SPM	lsim	1

temperature. In this simulation, the cell starts at 0 °C and, under adiabatic conditions, the temperature grows to 25 °C. Low temperature and low C-rate ($t < 200$ s) produces modest errors. Moderate C-rates at low temperatures produce large errors and high C-rates at higher temperatures produce the least errors.

To identify the working range of ESPM-T, we separate the C-rate and temperature effects by simulating constant hybrid pulse cycles at different temperatures. The temperature range is from −10 °C to 50 °C for 1 C, 2 C, 5 C, 7.5 C, 10 C, and 12.5 C constant hybrid 30 s pulse cycles. Figure 6 shows an example case of adiabatic simulation of 7.5 C–30 s pulse charge–discharge cycle. As the cell temperature increases with time, the initial voltage error between the AutoLion-ST and ESPM-T diminishes.

Figure 7 summarizes the maximum voltage error relative to AutoLion-ST at different C-rates versus cell temperature. Each curve is for a different C-rate pulse cycle as shown in Fig. 6(c). As the cell warms up due to cycling, the temperature increases and the maximum voltage error for the corresponding pulse is evaluated. The error eventually decreases with increasing temperature and decreasing C-rate, although the error increases slightly for $T > 25$ °C due to slight asymmetry between charge and discharge voltage errors. To maintain errors less than 1% requires $T > 17$ °C and $I < 5$ C. If 5% errors are acceptable then 12.5 C is possible for $T > 25$ °C and 1 C for $T > -10$ °C. The solid dot in Fig. 7 corresponds to the solid dot in Fig. 6(a).

Computation time of a 20 min simulation at 1 Hz sampling rate on an Intel® Core™ 2 Quad 2.4 GHz desktop computer of AutoLion-ST and other reduced-order models are shown in Table 2. ESPM and ESPM-T models are, respectively, 11.9 and 5 times faster than AutoLion-ST in this case.

4   Conclusion

The traditional SPM neglects electrolyte diffusion only provides satisfactory performance over narrow C-rate and temperature ranges. Using only seven states, the ESPM developed in this paper includes an IMA model of electrolyte diffusion and matches the AutoLion-ST pulse response up to 20 C at room temperature with 3% (62 mV) error. The ESPM linearized at 50% SOC, has slightly higher voltage error (4.3%/137 mV) for wider SOC swing (35–65%). The ESPM-T model updates the ESPM parameters with temperature, maintaining the voltage response to pulse charge–discharge current inputs to within 5% of the AutoLion-ST for 25 °C < T < 50 °C at 12.5 C and −10 °C < T < 50 °C at 1 C.

Appendix A: Submodel Coefficients

A.1 Coefficients of the Electrolyte Concentration Profile

$q_{1,n} = 36 D_n D_p D_s^2 \left(\varepsilon_n L_n + \varepsilon_s L_s + \varepsilon_p L_p \right)$

$q_{2,n} = 12 D_n D_s^2 L_p^2 \varepsilon_p \left(L_n \varepsilon_n + L_s \varepsilon_s \right) + 12 D_s^2 D_p L_n^2 \varepsilon_n \left(L_s \varepsilon_s + L_p \varepsilon_p \right) + 12 D_n D_s D_p L_s^2 \varepsilon_s \left(L_n \varepsilon_n + L_p \varepsilon_p \right)$

$\qquad + 36 D_n D_s D_p \varepsilon_n \varepsilon_p L_n L_s L_p$

$q_{3,n} = L_n L_s L_p \varepsilon_n \varepsilon_s \varepsilon_p \left[3 D_n D_p L_s^2 + 4 D_s^2 L_n L_p + 4 D_s L_s \left(D_n L_p + D_p L_n \right) \right]$

$p_{0,n} = p_{0,s} = p_{0,p} = 36 D_n D_p D_s^2 \left(L_n b_1 - L_p b_2 \right)$

$p_{1,n} = 12 D_n D_s L_n L_p b_1 \varepsilon_p \left(D_s L_p + 3 D_p L_s \right) + 12 D_n D_s L_s^2 \varepsilon_s \left(L_n b_1 + L_p b_2 \right) + \left[18 D_s^2 D_p b_1 \left(L_s \varepsilon_s + L_p \varepsilon_p \right) + 6 D_s^2 D_p L_p b_2 \varepsilon_n \right] \left(L_n^2 - x^2 \right)$

$p_{2,n} = L_p L_s \varepsilon_s \left[D_n L_n L_s b_1 \varepsilon_p \left(4 D_s L_p + 3 D_p L_s \right) + 6 D_s b_1 \varepsilon_p \left(D_s L_p + D_p L_s \right) \left(L_n^2 - x^2 \right) \right] + D_p D_s L_s b_2 \varepsilon_n \left(3 x^2 - L_n^2 \right)$

$p_{1,s} = 6 D_s \left[3 D_n D_p L_n b_1 \varepsilon_s \left(L_s^2 - x^2 \right) + 6 D_n D_p L_n^2 b_1 \varepsilon_s \left(L_s - x \right) + D_n D_p L_p b_2 \varepsilon_s \left(L_s^2 - 3 x^2 \right) + 2 D_n D_p L_s b_1 \varepsilon_s \left(L_s - 3 x \right) \right.$

$\qquad \left. + 3 D_n D_p L_n L_p b_2 \varepsilon_s \left(2 x - L_n \right) - 2 D_p D_s L_n^2 L_p b_2 \varepsilon_n + 6 D_n D_p L_n L_p \left(b_2 \varepsilon_n + b_1 \varepsilon_p \right) \left(L_n - x \right) + 2 D_n L_n L_p b_1 \varepsilon_p \left(D_s L_p + 3 D_p L_s \right) \right]$

$p_{2,s} = L_n L_p \varepsilon_s \left[3 D_n D_p L_s b_1 \varepsilon_p \left(L_s^2 + 3 x^2 \right) + 6 D_n D_p \left(L_n - x \right) \left(L_s^2 b_1 \varepsilon_p - L_s^2 b_2 \varepsilon_n \right) + 3 \left(L_n^2 + x^2 \right) \left(2 D_n D_p L_p b_1 \varepsilon_p - 2 D_s D_p L_n b_2 \varepsilon_n - 3 D_n D_p L_s b_2 \varepsilon_n \right) \right.$

$\qquad - \left\{ 12 D_n D_s L_p b_1 \varepsilon_p \left(L_s + L_n \right) + 18 D_n D_p L_n L_s \left(b_2 \varepsilon_n + b_1 \varepsilon_p \right) \right\} x + 2 D_p D_s L_n b_2 \varepsilon_n \left(6 L_n x + L_s^2 \right) + D_n b_1 \varepsilon_p \left\{ 4 D_s L_p L_s \left(3 L_n + L_s \right) \right.$

$\qquad \left. \left. + 9 D_p L_n^2 L_s \right\} \right]$

$p_{1,p} = 18 D_s^2 L_n L_p \left(D_n L_p b_1 \varepsilon_p - D_p L_n b_2 \varepsilon_n \right) - 6 D_n D_p D_s L_n L_s \left(b_1 L_s \varepsilon_s + 6 L_p b_2 \varepsilon_n \right) + 18 D_n D_s^2 \left[2 b_2 \left(L_n - x \right) \left(L_n L_p \varepsilon_n + L_s^2 \varepsilon_s \right) \right.$

$\qquad + 2 \left(L_s - x \right) \left(L_n^2 b_2 \varepsilon_n + L_n^2 b_1 \varepsilon_n + L_n L_p b_1 \varepsilon_s + L_s L_p b_2 \varepsilon_p \right) + 2 L_n L_s b_2 \left(L_p - x \right) \left(\varepsilon_n + \varepsilon_s \right) + L_n \left(b_2 \varepsilon_n + b_1 \varepsilon_p \right) \left(L_n^2 + x^2 \right)$

$\qquad \left. + L_s b_2 \varepsilon_s \left(b_2 \varepsilon_n + b_1 \varepsilon_p \right) \left(L_s^2 + x^2 \right) + L_n L_s \left(L_n b_2 \varepsilon_s + L_s b_2 \varepsilon_n + L_s b_1 \varepsilon_p \right) \right]$

$p_{2,p} = L_n L_s \varepsilon_s \left[3 D_n L_s b_2 \varepsilon_n \left(2 D_s L_n^2 - D_p L_p L_s \right) + 2 D_s L_n L_s b_2 \varepsilon_n \left(3 D_s L_s - 2 D_p L_p \right) - D_n D_s L_s b_1 \varepsilon_p \left(2 L_p^2 + 3 L_s^2 \right) \right.$

$\qquad + 6 D_n D_s L_s \left(2 L_p b_2 \varepsilon_n - L_s b_1 \varepsilon_p \right) \left(L_n - x \right) + 6 D_n D_s L_s \left(2 L_n b_2 \varepsilon_n - L_p b_1 \varepsilon_p \right) \left(L_s - x \right) + \left(12 D_s^2 L_n^2 b_2 \varepsilon_n + 12 D_s^2 L_n L_s b_2 \varepsilon_n + 12 D_n D_s L_s^2 b_2 \varepsilon_n \right.$

$\qquad \left. - 6 D_n D_s L_n L_s b_1 \varepsilon_p \right) \left(L_p - x \right) + 12 D_s^2 L_n b_2 \varepsilon_n \left(L_n L_s - x L_p \right) + \left(L_n^2 + x^2 \right) \left(6 D_s^2 L_n b_2 \varepsilon_n - 3 D_n D_s L_s b_1 \varepsilon_p \right) + 6 D_n D_s L_s b_2 \varepsilon_n \left(L_s^2 + x^2 \right) \right]$

A.2 Coefficients of Electrolyte Phase Potential Difference

$L_0 = 72 D_n D_p D_s^2 \kappa_n \kappa_p \kappa_s \left(L_n \varepsilon_n + L_s \varepsilon_s + L_p \varepsilon_p \right)$

$L_1 = 24 D_s \kappa_n \kappa_p \kappa_s \left[D_p D_s \varepsilon_n L_n^2 \left(\varepsilon_p L_p + \varepsilon_s L_s \right) + D_n \varepsilon_n \varepsilon_p L_n L_p \left(D_s L_p + 3 D_p L_s \right) + D_n \varepsilon_p \varepsilon_s L_p L_s \left(D_s L_p + D_p L_s \right) + D_n D_p \varepsilon_n \varepsilon_s L_n L_s^2 \right]$

$L_2 = 2 L_n L_p L_s \varepsilon_n \varepsilon_s \varepsilon_p \kappa_n \kappa_p \kappa_s \left(3 D_n D_p L_s^2 + 4 D_s^2 L_n L_p + 4 D_n D_s L_p L_s + 4 D_p D_s L_n L_s \right)$

$R_0 = 36 D_n D_p D_s^2 L_n^2 b_3 \kappa_p \kappa_s \left(L_n \varepsilon_n + L_s \varepsilon_s + L_p \varepsilon_p \right) - 36 D_n D_p D_s^2 L_p^2 b_4 \kappa_s \kappa_n^2 \left(L_n \varepsilon_n + L_s \varepsilon_s + L_p \varepsilon_p \right)$

$\qquad + 36 D_n D_s^2 L_p^2 b_2 \kappa_{d,p} \kappa_n \kappa_s \left(L_n \varepsilon_n + L_s \varepsilon_s \right) + 36 D_p D_s^2 L_n^2 b_1 \kappa_{d,n} \kappa_p \kappa_s \left(L_p \varepsilon_p + L_s \varepsilon_s \right) + 36 D_s^2 L_n L_p \kappa_s \left(D_p L_n b_2 \varepsilon_n \kappa_{d,n} \kappa_p + D_n L_p b_1 \varepsilon_p \kappa_{d,p} \kappa_n \right)$

$\qquad + 36 D_n D_p D_s L_s^2 \varepsilon_s \kappa_{d,s} \kappa_n \kappa_p \left(b_1 L_n + b_2 L_p \right) - 72 \left(D_n D_p D_s^2 L_p L_s b_4 \kappa_n^2 \kappa_p + D_n D_p D_s^2 L_n L_p b_4 \kappa_n \kappa_p \kappa_s \right) \left(L_n \varepsilon_n + L_s \varepsilon_s + L_p \varepsilon_p \right)$

$\qquad + 72 D_n D_p D_s L_n L_p L_s \kappa_{d,s} \kappa_n \kappa_p \left(b_2 \varepsilon_n + b_1 \varepsilon_p \right)$

$R_1 = 12 D_p D_s^2 L_n^2 \varepsilon_n \kappa_s \left(L_n^2 b_3 \kappa_p - L_p^2 b_4 \kappa_n \right) \left(L_p \varepsilon_p + L_s \varepsilon_s \right) + 12 D_n D_s^2 L_p^2 \kappa_s \left(L_n^2 b_3 \kappa_p \varepsilon_n - L_p^2 b_4 \kappa_n \varepsilon_p \right) \left(L_p \varepsilon_p + L_s \varepsilon_s \right)$

$\qquad + 12 D_n D_p D_s L_s^2 \varepsilon_s \kappa_s \left(L_n^2 b_3 \kappa_p - L_p^2 b_4 \kappa_n \right) \left(L_n \varepsilon_n + L_p \varepsilon_p \right) - 24 D_s^2 L_n L_p^2 b_4 \varepsilon_n \varepsilon_p \kappa_p \left(L_s \kappa_n + L_p \kappa_s \right) \left(D_n L_p + D_p L_n \right)$

$\qquad - 24 D_n D_s L_s L_p^2 b_4 \varepsilon_p \varepsilon_s \kappa_p \left(L_n \kappa_s + L_s \kappa_n \right) \left(D_s L_p + D_p L_s \right) - 24 D_p D_s L_n L_p L_s b_4 \varepsilon_n \varepsilon_s \kappa_p \left(L_n \kappa_s + L_s \kappa_n \right) \left(D_s L_n + D_n L_s \right)$

$\qquad - 72 D_n D_p D_s L_n L_p^2 L_s b_4 \varepsilon_n \varepsilon_p \kappa_p \left(L_s \kappa_n + L_n \kappa_s \right) + 12 D_s L_n L_p L_s^2 \varepsilon_s \kappa_{d,s} \kappa_n \kappa_p \left(D_p L_n b_2 \varepsilon_n + D_n L_p b_1 \varepsilon_p \right)$

$\qquad + 12 D_s^2 L_n^2 L_s L_p^2 \varepsilon_s \kappa_s \left(b_2 \varepsilon_n \kappa_n \kappa_{d,p} + b_1 \varepsilon_p \kappa_{d,n} \kappa_p \right) + 36 D_n D_p D_s L_n L_p \varepsilon_n \varepsilon_p \kappa_s \left(L_n^2 b_3 \kappa_n - L_p^2 b_4 \kappa_p \right)$

$\qquad + 6 D_n D_p L_n L_p L_s^3 \varepsilon_s \kappa_{d,s} \kappa_n \kappa_p \left(b_2 \varepsilon_n + b_1 \varepsilon_p \right) + 6 D_n D_s L_n L_p^2 L_s^2 \varepsilon_s \kappa_{d,p} \kappa_n \kappa_s \left(2 b_2 \varepsilon_n - b_1 \varepsilon_p \right)$

$\qquad - 6 D_p D_s L_n^2 L_p L_s^2 b_2 \varepsilon_n \varepsilon_s \kappa_{d,n} \kappa_p \kappa_s$

$R_2 = -L_n L_p L_s \varepsilon_n \varepsilon_s \varepsilon_p \left[\left(-b_3 \kappa_p \kappa_s L_n^2 + 2 b_4 \kappa_p \kappa_s \kappa_n L_n L_p + b_4 \kappa_s \kappa_n^2 L_p^2 + 2 b_4 \kappa_p \kappa_n^2 L_s L_p \right) \left(3 D_n D_p L_s^2 + 4 D_s^2 L_n L_p + 4 D_n D_s L_p L_s + 4 D_p D_s L_n L_s \right) \right]$

Appendix B: ESPM Impedance Transfer Function Derivation

Substituting Eqs. (33), (34), (36), (37), and (55) into Eq. (39), we obtain

$$\frac{\tilde{V}(s)}{I(s)} = K + \frac{R_2 s^2 + R_1 s + R_0}{L_2 s^2 + L_1 s + L_0} + \frac{\alpha_1 s^2 + 60\alpha_1\alpha_2 s + 495\alpha_1\alpha_2^2}{s^3 + 189\alpha_2 s^2 + 3465\alpha_2^2 s}$$
$$+ \frac{\beta_1 s^2 + 60\beta_1\beta_2 s + 495\beta_1\beta_2^2}{s^3 + 189\beta_2 s^2 + 3465\beta_2^2 s} \tag{B1}$$

where

$$K = -\left[\frac{R_{ct}^p}{a_s^p}\frac{1}{AL_p} + \frac{R_{ct}^n}{a_s^n}\frac{1}{AL_n} + \frac{R_c}{A}\right]$$

$$C^p = 21\frac{\partial U_p}{\partial c_{s,e}}$$

$$C^n = 21\frac{\partial U_n}{\partial c_{s,e}}$$

$$\alpha_1 = \frac{C^p}{a_s^p \mathrm{FAR}_s^p L_p}$$

$$\alpha_2 = \frac{D_s^p}{[R_s^p]^2}$$

$$\beta_1 = \frac{C^n}{a_s^n \mathrm{FAR}_s^n L_n}$$

$$\beta_2 = \frac{D_s^n}{[R_s^n]^2}.$$

Simplifying Eq. (B1)

$$\frac{\tilde{V}(s)}{I(s)} = K + \frac{E_0 s^2 + E_1 s + E_2}{s^2 + F_1 s + F_2} + \frac{A_2 s^2 + A_1 s + A_0}{s(s^2 + B_2 s + B_1)} + \frac{C_2 s^2 + C_1 s + C_0}{s(s^2 + D_2 s + D_1)} \tag{B2}$$

where

$$E_0 = \frac{R_2}{L_2}$$

$$E_1 = \frac{R_1}{L_2}$$

$$E_2 = \frac{R_0}{L_2}$$

$$F_1 = \frac{L_1}{L_2}$$

$$F_2 = \frac{L_0}{L_2}$$

$$A_0 = 495\alpha_1\alpha_2^2$$

$$A_1 = 60\alpha_1\alpha_2$$

$$A_2 = \alpha_1$$

$$B_1 = 3465\alpha_2^2$$

$$B_2 = 189\alpha_2$$

$$C_0 = 495\beta_1\beta_2^2$$

$$C_1 = 60\beta_1\beta_2$$

$$C_2 = \beta_1$$

$$D_1 = 3465\beta_2^2$$

$$D_2 = 189\beta_2$$

Factoring out one integrator, Eq. (B2) can be written as

$$\frac{\tilde{V}(s)}{I(s)} = K + \frac{K_1 + K_2}{s} + \frac{E_0 s^2 + E_1 s + E_2}{s^2 + F_1 s + F_2}$$
$$+ \frac{g_1 s^3 + g_2 s^2 + g_3 s + g_4}{s^4 + h_1 s^3 + h_2 s^2 + h_3 s + h_4} \tag{B3}$$

where

$$K_1 = \frac{A_0}{B_1}$$

$$e_0 = \frac{A_1 B_1 - A_0 B_2}{B_1}$$

$$e_1 = \frac{A_2 B_1 - A_0}{B_1}$$

$$K_2 = \frac{C_0}{D_1}$$

$$f_0 = \frac{C_1 D_1 - C_0 D_2}{D_1}$$

$$f_1 = \frac{C_2 D_1 - C_0}{D_1}$$

$$g_1 = e_1 + f_1$$

$$g_2 = e_0 + e_1 D_2 + f_0 + f_1 B_2$$

$$g_3 = e_0 D_2 + e_1 D_1 + f_0 B_2 + f_1 B_1$$

$$g_4 = e_0 D1 + f_0 B1$$

$$h_1 = B_2 + D_2$$

$$h_2 = B_1 + B_2 D_2 + D_1$$

$$h_3 = B_1 D_2 + B_2 D_1$$

$$h_4 = B_1 D_1$$

After further manipulation of Eq. (B3), the final equation suitable for state space realization can be written as follows:

$$\frac{\tilde{V}(s)}{I(s)} = K + \frac{K_1 + K_2}{s}$$
$$+ \frac{b_{00} s^6 + b_{01} s^5 + b_{02} s^4 + b_{03} s^3 + b_{04} s^2 + b_{05} s + b_{06}}{s^6 + a_{01} s^5 + a_{02} s^4 + a_{03} s^3 + a_{04} s^2 + a_{05} s + a_{06}} \tag{B4}$$

where

$$b_{00} = E_0$$

$$b_{01} = E_1 + g_1 + E_0 h_1$$

$$b_{02} = E_2 + g_2 + E_0 h_2 + E_1 h_1 + F_1 g_1$$

$$b_{03} = g_3 + E_0 h_3 + E_1 h_2 + E_2 h_1 + F_1 g_2 + F_2 g_1$$

$$b_{04} = g_4 + E_0 h_4 + E_1 h_3 + E_2 h_2 + F_1 g_3 + F_2 g_2$$

$$b_{05} = E_1 h_4 + E_2 h_3 + F_1 g_4 + F_2 g_3$$

$$b_{06} = E_2 h_4 + F_2 g_4$$

$$a_{01} = F_1 + h_1, \quad a_{02} = F_2 + h_2 + F_1 h_1$$

$$a_{03} = h_3 + F_1 h_2 + F_2 h_1$$

$$a_{04} = h_4 + F_1 h_3 + F_2 h_2$$

$$a_{05} = F_1 h_4 + F_2 h_3$$

$$a_{06} = F_2 h_4$$

References

[1] Office of the Press Secretary, 2013, *The White House Press Release*, Washington, DC, http://www.whitehouse.gov/the-press-office

[2] Thomas, C. E. S., 2009, "Transportation Options in a Carbon-Constrained World: Hybrids, Plug-In Hybrids, Biofuels, Fuel Cell Electric Vehicles, and Battery Electric Vehicles," Int. J. Hydrogen Energy, **34**(23), pp. 9279–9296.

[3] Rahn, C. D., and Wang, C. Y., 2013, *Battery Systems Engineering*, Wiley, State College, PA.

[4] Plett, G. L., 2004, "Extended Kalman Filtering for Battery Management Systems of LiPB-Based HEV Battery Packs Part 1. Background," J. Power Sources, **134**(2), pp. 252–261.

[5] Plett, G. L., 2004, "Extended Kalman Filtering for Battery Management Systems of LiPB-Based HEV Battery Packs Part 2. Modeling and Identification," J. Power Sources, **134**(2), pp. 262–276.

[6] Plett, G. L., 2004, "Extended Kalman Filtering for Battery Management Systems of LiPB-Based HEV Battery Packs Part 3. State and Parameter Estimation," J. Power Sources, **134**(2), pp. 277–292.

[7] Verbrugge, M. W., and Conell, R. S., 2002, "Electrochemical and Thermal Characterization of Battery Modules Commensurate With Electric Vehicle Integration," J. Electrochem. Soc., **149**(1), pp. A45–A53.

[8] Verbrugge, M. W., and Liu, P., 2007, "Electrochemical Characterization of High-Power Lithium Ion Batteries Using Triangular Voltage and Current Excitation Sources," J. Power Sources, **174**(1), pp. 2–8.

[9] Schweighofer, B., Raab, K. M., and Brasseur, G., 2003, "Modeling of High Power Automotive Batteries by the Use of an Automated Test System," IEEE Trans. Instrum. Meas., **52**(4), pp. 1087–1091.

[10] Moss, P. L., Au, G., Plichta, E. J., and Zheng, J. P., 2008, "An Electrical Circuit for Modeling the Dynamic Response of Li-Ion Polymer Batteries," J. Electrochem. Soc., **155**(12), pp. A986–A994.

[11] Smith, K. A., Rahn, C. D., and Wang, C. Y., 2007, "Control Oriented 1D Electrochemical Model of Lithium Ion Battery," Energy Convers. Manage., **48**(9), pp. 2565–2578.

[12] Smith, K. A., Rahn, C. D., and Wang, C. Y., 2008, "Model Order Reduction of 1D Diffusion Systems Via Residue Grouping," ASME J Dyn. Syst. Meas. Control, **130**(5), p. 011012.

[13] Doyle, M., and Newman, J., 1996, "Comparison of Modeling Predictions With Experimental Data From Plastic Lithium Ion Cells," J. Electrochem. Soc., **143**(6), pp. 1890–1903.

[14] Doyle, M., and Fuentes, Y., 2003, "Computer Simulations of a Lithium-Ion Polymer Battery and Implications for Higher Capacity Next-Generation Battery Designs," J. Electrochem. Soc., **150**(6), pp. A706–A713.

[15] Gu, W. B., and Wang, C. Y., 2000, "Thermal-Electrochemical Modeling of Battery Systems," J. Electrochem. Soc., **147**(8), pp. 2910–2922.

[16] Smith, K. A., Rahn, C. D., and Wang, C. Y., 2010, "Model-Based Electrochemical Estimation and Constraint Management for Pulse Operation of Lithium Ion Batteries," IEEE Trans. Control Syst. Technol., **18**(3), pp. 654–663.

[17] Prasad, G. K., and Rahn, C. D., 2012, "Development of a First Principles Equivalent Circuit Model for a Lithium Ion Battery," ASME Paper No. DSCC2012-MOVIC2012-8607.

[18] Lee, J. L., Chemistruck, A., and Plett, G. L., 2012, "One-Dimensional Physics-Based Reduced-Order Model of Lithium-Ion Dynamics," J. Power Sources, **220**, pp. 430–448.

[19] Klein, R., Chaturvedi, N. A., Christensen, J., Ahmed, J., Findeisen, R., and Kojic, A., 2010, "State Estimation of a Reduced Electrochemical Model of a Lithium-Ion Battery," American Control Conference, Baltimore, MD, June 30–July 2, pp. 6618–6623.

[20] Klein, R., Chaturvedi, N. A., Christensen, J., Ahmed, J., Findeisen, R., and Kojic, A., 2013, "Electrochemical Model Based Observer Design for a Lithium-Ion Battery," IEEE Trans. Control Syst. Technol., **21**(2), pp. 289–301.

[21] Haran, B. S., Popov, B. N., and White, R. E., 1998, "Determination of the Hydrogen Diffusion Coefficient in Metal Hydrides by Impedance Spectroscopy," J. Power Sources, **75**(1), pp. 56–63.

[22] Chaturvedi, N. A., Klein, R., Christensen, J., Ahmed, J., and Kojic, A., 2010, "Algorithms for Advanced Battery-Management Systems," IEEE Control Syst. Mag., **30**(3), pp. 49–68.

[23] Moura, S. J., Chaturvedi, N. A., and Krstić, M., 2012, "PDE Estimation Techniques for Advanced Battery Management Systems—Part I: SOC Estimation," American Control Conference, Montreal, QC, Canada, June 27–29, pp. 559–565.

[24] Santhanagopalan, S., Guo, Q., Ramadass, P., and White, R. E., 2006, "Review of Models for Predicting the Cycling Performance of Lithium Ion Batteries," J. Power Sources, **156**(2), pp. 620–628.

[25] Rahimian, S. K., Rayman, S., and White, R. E., 2013, "Extension of Physics-Based Single Particle Model for Higher Charge–Discharge Rates," J. Power Sources, **224**, pp. 180–194.

[26] Marcicki, J., Canova, M., Conlisk, A. T., and Rizzoni, G., 2013, "Design and Parametrization Analysis of a Reduced-Order Electrochemical Model of Graphite/LiFeO$_4$ Cells for SOC/SOH Estimation," J. Power Sources, **237**, pp. 310–324.

[27] Christofides, P. D., and Daoutidis, P., 1997, "Finite-Dimensional Control of Parabolic PDE Systems Using Approximate Inertial Manifolds," J. Math. Anal. Appl., **216**(2), pp. 398–420.

[28] Baker, J., and Christofides, P. D., 2000, "Finite-Dimensional Approximation and Control of Nonlinear Parabolic PDE Systems," Int. J. Contr., **73**(5), pp. 439–456.

[29] Verbrugge, M. W., and Koch, B. J., 2003, "Electrochemical Analysis of Lithiated Graphite Anodes," J. Electrochem. Soc., **150**(3), pp. A374–A384.

[30] Yabuuchi, N., Makimura, Y., and Ohzuku, T., 2007, "Solid-State Chemistry and Electrochemistry of LiCo$_{1/3}$Ni$_{1/3}$Mn$_{1/3}$O$_2$ for Advanced Lithium-Ion Batteries III. Rechargeable Capacity and Cycleability," J. Electrochem. Soc, **154**(4), pp. A314–A115.

[31] Fang, W., Kwon, O. J., and Wang, C. Y., 2010, "Electrochemical–Thermal Modeling of Automotive Li-Ion Batteries and Experimental Validation Using a Three-Electrode Cell," Int. J. Energy Res., **34**(2), pp. 107–115.

[32] Ji, Y., Zhang, Y., and Wang, C. Y., 2013, "Li-Ion Cell Operation at Low Temperatures," J. Electrochem. Soc, **160**(4), pp. A636–A649.

[33] Jacobsen, T., and West, K., 1995, "Diffusion Impedance in Planar, Cylindrical and Spherical Symmetry," Electrochem. Acta, **40**(2), pp. 255–262.

[34] Forman, J. C., Bashash, S., Stein, J. L., and Fathy, H. K., 2011, "Reduction of an Electrochemistry-Based Li-Ion Battery Model Via Quasi-Linearization and Padé Approximation," J. Electrochem. Soc., **158**(2), pp. A93–A101.

[35] Shi, Y., Prasad, G. K., Shen, Z., and Rahn, C. D., 2011, "Discretization Methods for Battery Systems Modeling," American Control Conference, CA.

[36] Gebhart, B., 1993, *Heat Conduction and Mass Diffusion*, McGraw-Hill, New York.

[37] Subramanian, V. R., Ritter, J. A., and White, R. E., 2001, "Approximate Solutions for Galvanostatic Discharge of Spherical Particles," J. Electrochem. Soc., **148**(11), pp. E444–E449.

[38] Subramanian, V. R., Tapriyal, D., and White, R. E., 2004, "A Boundary Condition for Porous Electrodes," Electrochem. Solid State Lett., **7**(9), pp. A259–A263.

[39] Frankline, G. F., Powell, J. D., and Naeini, A. E., 2011, *Feedback Control of Dynamic Systems*, Pearson, New Delhi, India.

[40] Valøen, L. O., and Reimers, J. N., 2005, "Transport Properties of LiPF$_6$-Based Li-Ion Battery Electrolytes," J. Electrochem. Soc., **152**(5), pp. A882–A891.

[41] EC Power, 2013, "Software Products," http://ecpowergroup.com/products-2/software-licensing